
Subarcsecond imaging of a solar active region filament with ALMA and IRIS

J. M. da Silva Santos^{1,*}, S. M. White², K. Reardon¹, G. Cauzzi¹, S. Gunár³, P. Heinzel³, and J. Leenaarts⁴

¹*National Solar Observatory, Boulder, CO, USA*

²*Space Vehicles Directorate, Air Force Research Laboratory, Albuquerque, NM, USA*

³*Astronomical Institute of the Czech Academy of Sciences, Ondřejov, Czech Republic*

⁴*Institute for Solar Physics, Department of Astronomy, Stockholm University, Stockholm, Sweden*

Correspondence*:
3665 Discovery Drive, Boulder 80303, CO, USA
jdasilvasantos@nso.edu

ABSTRACT

Quiescent filaments appear as absorption features on the solar disk when observed in chromospheric lines and at continuum wavelengths in the millimeter (mm) range. Active region (AR) filaments are their small-scale, low-altitude analogues, but they could not be resolved in previous mm observations. This spectral diagnostic can provide insight into the details of the formation and physical properties of their fine threads, which are still not fully understood. Here, we shed light on the thermal structure of an AR filament using high-resolution brightness temperature (T_b) maps taken with ALMA Band 6 complemented by simultaneous IRIS near-UV spectra, Hinode/SOT photospheric magnetograms, and SDO/AIA extreme-UV images. Some of the dark threads visible in the AIA 304 Å passband and in the core of Mg II resonance lines have dark ($T_b < 5000$ K) counterparts in the 1.25 mm maps, but their visibility significantly varies across the filament spine and in time. These opacity changes are possibly related to variations in temperature and electron density in filament fine structures. The coolest T_b values (< 5000 K) coincide with regions of low integrated intensity in the Mg II h and k lines. ALMA Band 3 maps taken after the Band 6 ones do not clearly show the filament structure, contrary to the expectation that the contrast should increase at longer wavelengths based on previous observations of quiescent filaments. The ALMA maps are not consistent with isothermal conditions, but the temporal evolution of the filament may partly account for this.

Keywords: Sun, radio, ultraviolet, chromosphere, active regions, filaments, prominences

1 INTRODUCTION

Dark filaments on the solar disk and bright prominences at the limb are homologous structures filled with cool ($\lesssim 10^4$ K), dense plasma suspended by the Lorentz force against gravity above polarity-inversion lines in the photosphere. They are generally separated into two categories: the larger ($\sim 10 - 100$ Mm), long-lived, high-altitude (> 10 Mm) quiescent filaments and the smaller (~ 10 Mm), more dynamic, lower-altitude (< 10 Mm) active region (AR) filaments. The magnetic field in the former is essentially horizontal with field strengths of $\sim 3-80$ G (Leroy, 1989; Casini et al., 2005; Orozco Suárez et al., 2014), but AR filaments may show flux rope structure and field strengths that can be an order of magnitude higher than in the quiescent ones (Kuckein et al., 2009, 2012; Guo et al., 2010; Xu et al., 2012; Díaz Baso et al., 2019). Estimates of (core) kinetic temperatures in prominences lie within the range $\sim 5\,000 - 9\,000$ K for microturbulence values within $\sim 3 - 16$ km s $^{-1}$ (e.g., Stellmacher et al., 2003; Jejič et al., 2018; Ruan et al., 2019). While the general properties of filaments are well understood, there are open questions pertaining to their fine structure and magnetic configuration (Chen et al., 2020, and references therein). Furthermore, they may become unstable and erupt, leading to coronal mass ejections, hence their relevance in the context of solar activity and space weather (see reviews by Parenti, 2014; Gibson, 2018).

Observational studies have mainly used spectral lines such as Ly α , H α , Ca II H, 8542 Å, He I D₃, 10830 Å, and He II 304 Å to investigate prominence/filament thermodynamics and to infer the magnetic field topology (e.g., Labrosse et al., 2010, and references therein). These structures have also been routinely observed in the last decade by the Interface Region Imaging Spectrograph (IRIS, De Pontieu et al., 2014) in the Mg II h and k resonance lines, which have been used to investigate dynamics in prominences (e.g. Schmieder et al., 2014) and constrain nonlocal thermodynamic equilibrium (non-LTE) models (Heinzl et al., 2015b; Vial et al., 2019; Levens and Labrosse, 2019; Peat et al., 2021). Similar studies have yet to be conducted for AR filaments.

At the other end of the wavelength spectrum, low-resolution ($> 20''$) radio observations have shown that quiescent filaments appear as depressions of the background brightness temperatures on disk at continuum wavelengths between 3–8 mm, possibly due to free-free absorption by dense, cool material, and as emission features at the limb (Kundu, 1972; Raoult et al., 1979; Schmahl et al., 1981; Vrsnak et al., 1992). At wavelengths around 1 mm, prominences are still well visible at the limb (Harrison et al., 1993), but they are practically invisible on disk (Bastian et al., 1993; Lindsey, 1994). Under certain conditions, brightness measurements at different mm wavelengths can be used to constrain the optical thickness and kinetic temperature of such structures (Heinzl et al., 2015a; Rodger and Labrosse, 2017; Gunár et al., 2018).

The Atacama Large Millimeter/submillimeter Array (ALMA, Wootten and Thompson, 2009) provides an opportunity to investigate filament substructure in the (thermal) millimeter continuum at a much higher spatial resolution than before (see review by Wedemeyer et al., 2016). These capabilities have been recently demonstrated for a prominence at the limb (Heinzl et al., 2022; Labrosse et al., 2022). The only ALMA observations of filaments available until now have been taken with single dishes with a beam size of approximately $25''$ at 1.25 mm (White et al., 2017; Alissandrakis et al., 2017; Brajša et al., 2018). Here, we use interferometry maps with a significantly improved spatial resolution ($\sim 0.6''$ at 1.25 mm) that show considerably lower brightness temperatures in an AR filament compared to the background. Because of their smaller spatial scales, AR filaments had not yet been observed in this wavelength range. We compare the ALMA maps to UV imagery provided by IRIS and the Solar Dynamics Observatory (SDO, Pesnell et al., 2012) and magnetograms obtained by the Solar Optical Telescope (SOT, Tsuneta et al., 2008) onboard Hinode.

2 OBSERVATIONS

We observed NOAA AR 12738 on April 13, 2019, with ALMA Band 6 (240 GHz or 1.25 mm) in two execution blocks between 14:15-15:10 UT and 16:52-17:47 UT in mosaic mode and with Band 3 (100 GHz or 3 mm) in two execution blocks between 18:19-18:54 UT and 19:15-19:50 UT in single-pointing mode. The target was a group of pores and plage region near the disk center at $\mu \approx 0.98$ (the cosine of the heliocentric angle), west of a leading sunspot, where an AR filament was also visible for most of the observing campaign. We obtained co-temporal observations with IRIS and Hinode for the first Band 6 block and part of the second block. There are no IRIS nor Hinode supporting observations to the ALMA Band 3 data. We also use full-disk images in the ultraviolet range taken by the Atmospheric Imaging Assembly (AIA, Lemen et al., 2012) and continuum images at 6163 Å obtained by the Helioseismic and Magnetic Imager (HMI, Scherrer et al., 2012) on SDO. We use one H α image taken by the Global Oscillation Network Group (GONG, Harvey et al., 2011).

2.1 Data reduction and calibration

The ALMA array consisted of 9×7 m and 40×12 m functioning antennas, with a maximum baseline length of about 700 m. In order to cover a significant region of plage, a mosaic of ten different pointings was carried out using Band 6, covering a region slightly larger than 1 arcminute across, which is comparable to the Band 3 field of view (FOV). The FOV of a 12 m antenna is $25''$ at 230 GHz, and the centers of adjacent mosaic fields have a separation of $12''$. The observation cycled through the ten mosaic fields in order, acquiring three 2 s integrations at each visit. The duration of a full mosaic cycle was 85 s; these were repeated during scans on the Sun approximately 7-min long alternating with 2-min calibration scans.

We attempted to make time-resolved images of complete mosaic cycles using the standard Common Astronomy Software Applications (CASA, McMullin et al., 2007) package, applying the recommended "mosaic" gridding option, but we found that most of the resulting images were corrupted by bright or dark features at the edges of the mosaic. This did not occur when the full-time range was mapped. To get around this problem, we mapped and self-calibrated every integration in every field separately without primary beam correction, including the four base bands at 230, 232, 245 and 247 GHz to improve uv coverage, and then combined them in a linear mosaic in the image plane, weighting overlapping regions of the image using the appropriate primary beam response for the 12 m antennas. The single-field images were restored with a Gaussian beam with full-width-at-half-maximum of $0.6''$. The three consecutive integrations at each pointing were combined, and at each step, the time-dependent mosaic image was created by replacing the previous image of the current field with the new image, appropriately weighted by the primary beam, and recalculating the mosaic. This resulted in a sequence of 280 mosaic images for each of the two observations with a time separation of 9 s between mosaics within a scan, but the true time resolution is more complicated due to the overlapping nature of the fields. Comparison of the resulting images with cases where CASA successfully imaged a full 85 s mosaic cycle indicated good agreement.

The Band 6 mosaics were scaled to T_b units, and a value of 6 600 K was added to the mosaics to compensate for the background level not observable by the interferometer, derived by inspection of the corresponding FOV in single-dish images (taken with the total-power array) that measure the full solar disk temperatures. The typical temperature range in individual mosaic images is from $\sim 4\,000$ to $\sim 8\,500$ K.

The Band 3 data consists of single-pointing maps at 2-s cadence, maximum spatial resolution of $1.2''$, and noise level of 20 K. We refer to da Silva Santos et al. (2020) for a detailed explanation of the data reduction, which includes self-calibration, primary beam correction, and absolute flux calibration.

The SDO level 1 data were converted into level 1.5 using the `aia_prep` routine in SolarSoftWare (SSW, Freeland and Handy, 1998). Further processing including coalignment, resampling, and derotation was performed using the `SunPy` package (The SunPy Community et al., 2020). The HMI 6173 Å continuum images were deconvolved using the `Enhance` deep learning code¹ (Díaz Baso and Asensio Ramos, 2018). The AIA 304 Å images were corrected for stray light using semi-empirical point-spread functions (Poduval et al., 2013) and instrumental degradation. The data cadences are 12 s and 24 s in the EUV and UV.

The IRIS data comprises a time series of dense 64-step raster scans in the near-UV and far-UV wavelength ranges. Here we only use the spectral data around the Mg II h and k lines that probe the chromosphere; there is no signal in the far-UV lines in the filament. The pixel scale is 0.166'' along the slit and the size of the FOV is 22'' × 67''. The integration time was 1 s and the raster cadence was about 2.3 min. The level 2 data were converted from data units into intensity in physical units using version five of the spectrograph effective areas obtained through the `iris_get_response` routine in SSW.

The Hinode/SOT data consists of level 2 products, which include the magnetic field strength ($|B|$), the stray-light filling factor ($1 - f$), inclination (γ), and azimuth (ϕ) angles derived from Milne-Eddington inversions of the Fe I 6301.5 and 6302.5 Å Zeeman sensitive lines (Lites and Ichimoto, 2013). The line of sight (LOS) component of the magnetic field vector is given by $B_{\text{LOS}} = (1 - f)|B| \cos(\gamma)$. The slit step is $\sim 0.297''$ and the pixel scale is $\sim 0.319''$ along the slit. The size of the FOV is approximately 60'' × 61''. The exposure time was 1.6 s and the raster cadence was ~ 13 min.

The co-alignment of the IRIS and Hinode data was improved by cross-correlation with the HMI continuum images. The ALMA Band 6 maps were cross-correlated with AIA 304 Å images taken at an instant close to the middle of each ALMA mosaic sampled at the same spatial resolution. This allowed a proper coalignment of the EUV and mm brightenings recurring near the pore at the center of the FOV (not displayed; see also da Silva Santos et al., 2020).

2.2 Data clustering

To investigate the spatial correlation between the Mg II h and k profiles and the mm continuum emission, we applied an agglomerative hierarchical clustering method to the former using the `hierarchy` library in `Scipy` (Virtanen et al., 2020) wherein profiles are grouped based on a distance metric. We used Ward's linkage method, which minimizes the within-cluster variance (Ward, 1963), that is the spread in the euclidean distances between each cluster member and the centroid. This technique can be interpreted as a type of dimensionality reduction in that the information in the IRIS spectra with hundreds of wavelength points is condensed into a single number, which can then be compared to the 1.25 mm continuum brightness. The number of clusters was decided upon visual inspection of the dendrogram. While that choice is arbitrary, we concluded that 15 clusters were a good compromise between limiting the impact of noise and being able to identify sufficient spatial structure within the filament while tracking its time evolution. The clustering is based on 20475 spectral profiles of the wavelength window between 2791.2–2809.6 Å, which includes the Mg II h, k, and UV triplet lines.

3 RESULTS

Figure 1 shows the target as observed by the different instruments at the start of the coordinated campaign. Observations of this AR with ALMA have shown that $T_b(3\text{ mm})$ correlates poorly with AIA 1600 Å intensity ($r = 0.34$, da Silva Santos et al., 2020). Here, we find that $T_b(1.25\text{ mm})$ correlates

¹ <https://github.com/cdiazbas/enhance>

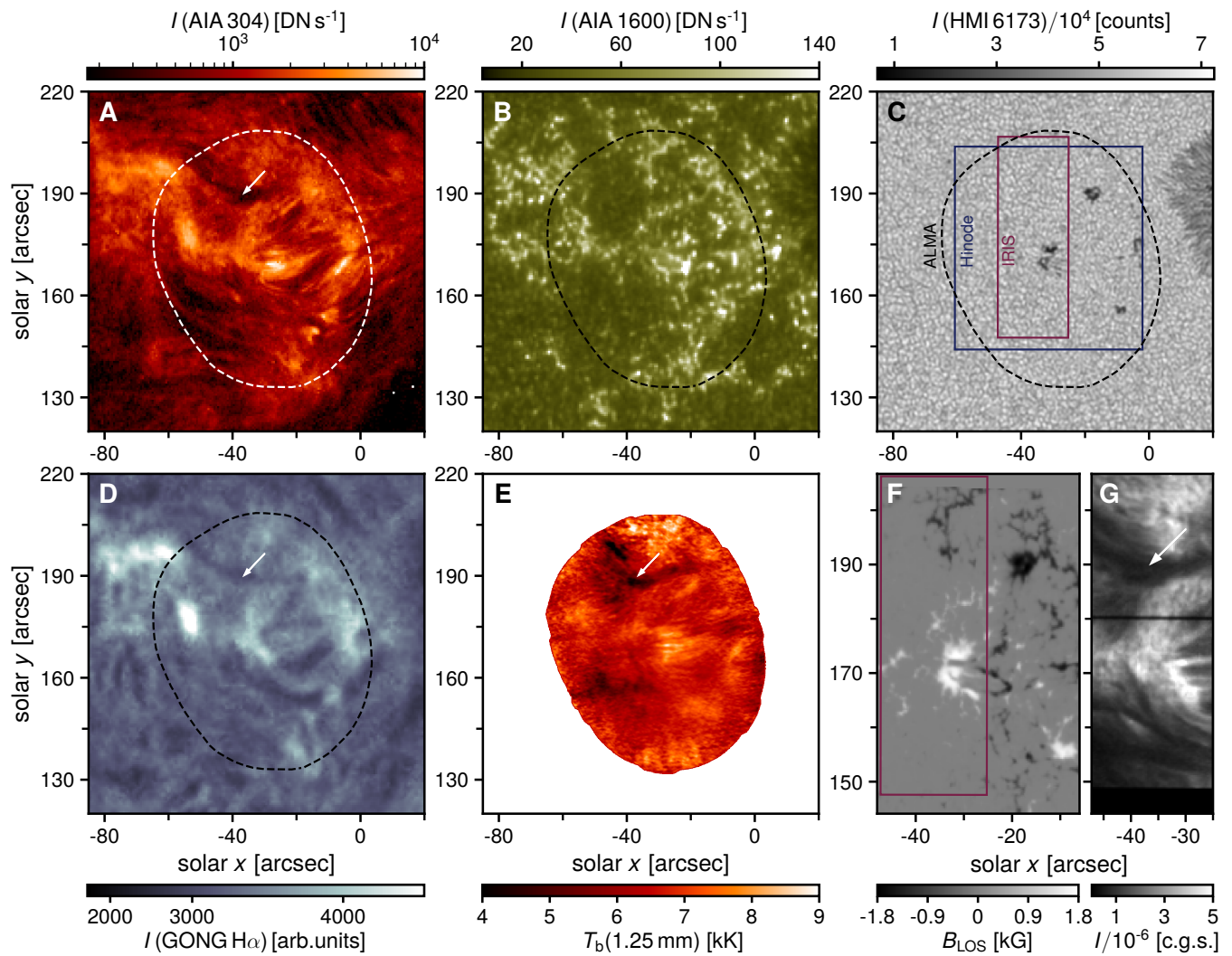


Figure 1. Overview of NOAA AR 12738 by different instruments on April 13, 2019, around 14:15 UT. Panel A: SDO/AIA 304 Å intensity in logarithmic scale; panel B: SDO/AIA 1600 Å intensity (capped); panel C: deconvolved SDO/HMI 6173 Å continuum intensity; panel D: gamma-adjusted and unsharpened GONG H α ; panel E: ALMA Band 6 brightness temperature mosaic; panel F: Hinode/SOT line-of-sight magnetogram; panel G: IRIS intensity in the core of Mg II k (in units of $\text{erg s}^{-1}\text{sr}^{-1}\text{cm}^{-2}\text{Hz}^{-1}$). The dashed lines show the ALMA field of view, and the boxes in panel C show the area covered by the Hinode and IRIS raster scans. The arrows indicate the location of an AR filament.

slightly better with AIA 1600 Å emission ($r = 0.45$), which is consistent with lower formation heights of shorter mm wavelengths. An overall better agreement is found with the AIA 304 Å intensities, especially during small-scale transient brightenings similarly to the ones observed with Band 3 (da Silva Santos et al., 2020), but we did not quantify this correlation as the main focus of this paper is the AR filament described below.

The observations also reveal a dark filamentary structure that can be identified in all of the chromospheric diagnostics in the upper part of the FOV. However, the filament appears fragmented into pieces at 1.25 mm in contrast with the more uniform dark structures seen in H α , He I 304 Å, and Mg II k. Brightness values as low as $T_b(1.25 \text{ mm}) \sim 2800 \text{ K}$ can be found at certain locations, but other parts of the filament cannot be distinguished from the background, suggesting either significant opacity variations or temperature

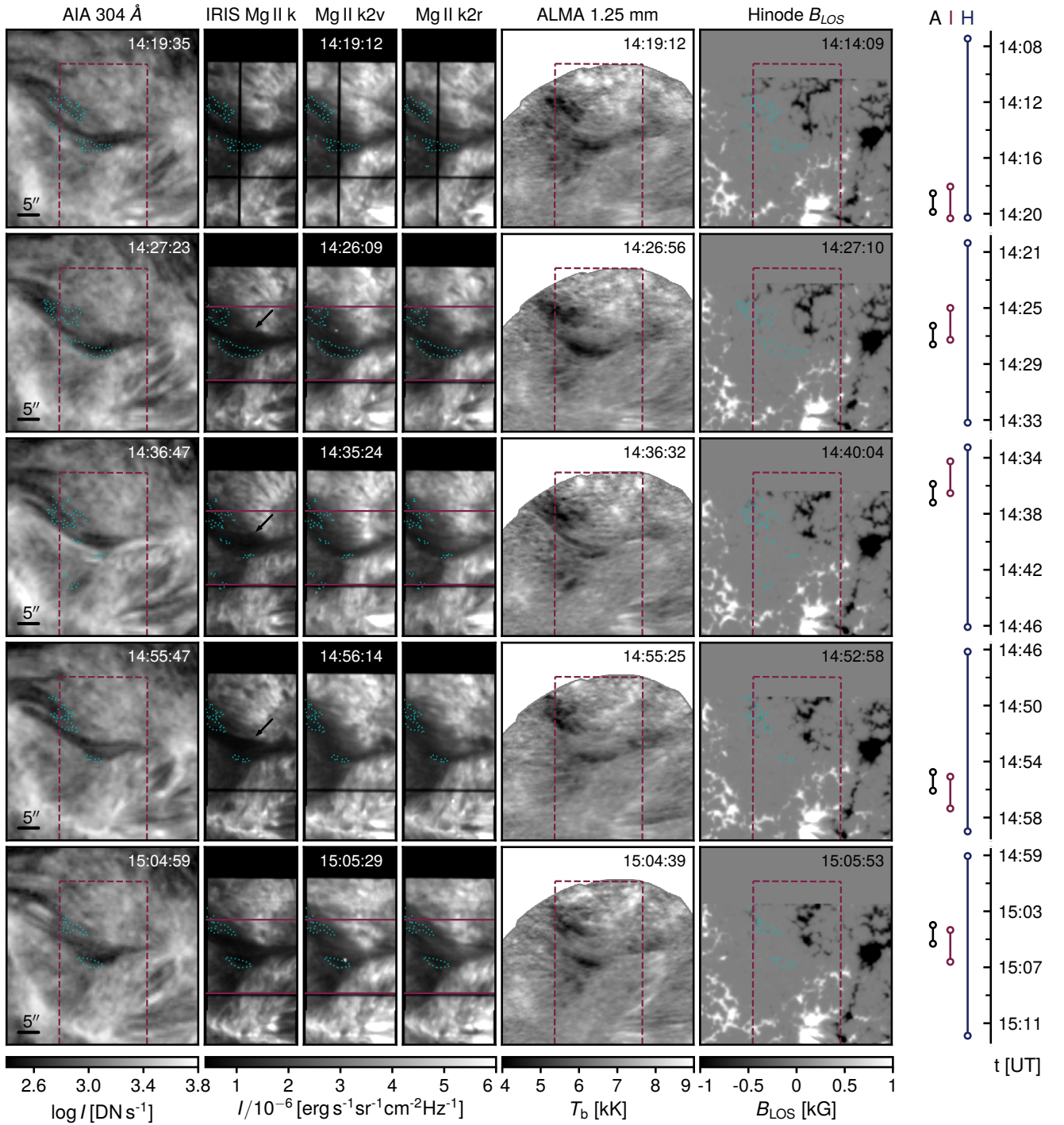


Figure 2. Time evolution of the AR filament. The AIA 304 Å images have been averaged within the time span needed by ALMA to mosaic the filament. The intensities are capped for display purposes. The time stamps on the IRIS and Hinode raster images correspond to the central slit position. The dashed boxes show the IRIS FOV. The cyan contours show $T_b(1.25 \text{ mm}) = 5000 \text{ K}$. The horizontal magenta lines delimit the area displayed in Fig. 3. The data acquisition times are shown on the right.

variations if the filament threads are optically thick. Other dark $H\alpha$ fibrils near the center of the ALMA FOV appear to have no counterpart at 1.25 mm.

Figure 2 shows the temporal evolution of the filament as seen by the different instruments. The y -axes in all panels are aligned with solar north. The appearance of the filament in the Band 6 maps changes dramatically over one hour as parts of it practically vanish and reappear, whereas the filament spine remains well visible in the Mg II core images throughout. The dark Band 6 structures thin out around 14:36 UT when a bright thread forms in the 304 Å images, following a brightening at the eastern footpoint of the filament. The lowest $T_b(1.25 \text{ mm})$ values ($<5000 \text{ K}$) are located near the widest part of the filament but usually offset from the darkest regions in the 304 Å images. We find that the coolest $T_b(1.25 \text{ mm})$ values correlate with the darkest features in the k2v and k2r images, whereas the dark clouds in the core of the h and k lines (as indicated by the arrows), which probes higher heights, are indistinguishable from the background at 1.25 mm. Note that depending on the phase of the IRIS slit-scan, there could be a time lag of up to ~ 1.5 min between the latter and ALMA. Even in the darkest part of the filament, the intensities in the core of the Mg II lines are about 10–15% brighter than the mean QS profile at disk center, yet the filament contrast is high owing to the bright surrounding plage. The SOT magnetograms do not show a significant change in the photospheric magnetic flux underneath the filament spine over time.

Figure 3 shows the results of the clustering algorithm on the IRIS spectra. To create smooth spatial maps of cluster types, profiles belonging to a particular cluster were averaged, and the 15 mean spectra were sorted in terms of integrated intensity (within $\pm 50 \text{ km s}^{-1}$ from line center) and labeled from A to O; a few of those profiles are displayed for comparison. A simple intensity threshold of 650 DN s^{-1} separates well the filament structure from the background in the AIA 304 Å passband. The coolest $T_b(1.25 \text{ mm})$ values ($<5000 \text{ K}$ contours) occur in regions where, on average, the Mg II h and k lines are the narrowest, the central reversals are the shallowest, and the h and k double peaks are more symmetric, which suggests small velocity gradients. The average k line width measured at half intensity between the averaged k2v and k2r peaks and the averaged k1r and k1v dips is $\approx 0.31 \text{ Å}$ compared to $\approx 0.54 \text{ Å}$ in the nearby plage (e.g., profile N). The filament body north of the Band 6 contours shows Mg II profiles that are just as dark in the h and k cores as in the lower part (cf. Fig. 2), but they are broader and show stronger, more asymmetrical, and separated k2v and k2r (or h2v, h2r) peaks, so they are classified as a different type. This implies that the coolest Band 6 temperatures coincide with the regions of lower integrated intensity in the h and k lines where the coolest and densest material may be located.

The aforementioned trend generally holds at different times but the time lag between the mm and NUV diagnostics has to be taken into consideration. At 14:26, low $T_b(1.25 \text{ mm})$ values coincide with locations with A- and B-type IRIS profiles – they are essentially of the same kind but B-types are only slightly broader and brighter. These profiles practically disappear at 14:35, so do $T_b(1.25 \text{ mm}) < 5000 \text{ K}$; this appears to be related to the heating event that occurs along the filament spine as shown by the 304 Å image; both signatures reappear at 15:05. We note that there are locations outside of the filament that show A- or B-type profiles where low $T_b(1.25 \text{ mm})$ values are not found, and vice-versa, which just indicates relative, spatially-dependent opacity variations in both diagnostics.

Figure 4 shows selected ALMA Band 3 maps obtained after the Band 6 mosaics. The AIA images show a more dramatic evolution of the filament compared to an earlier time in the day (cf. Fig. 2), to the point that the filament practically vanished towards the end of the second observing block. Unlike the 1.25 mm maps, the 3 mm maps do not show the same dark features against the background. This is interesting in that the optical thickness is expected to increase with wavelength, so the absorbing features in Band 6 should appear even darker in Band 3, that is the contrast is expected to slightly increase at longer wavelengths by extrapolation of the contrast curve obtained from previous low-resolution observations of quiescent filaments in the mm and cm ranges (Raoult et al., 1979). Therefore, it is somewhat surprising that the

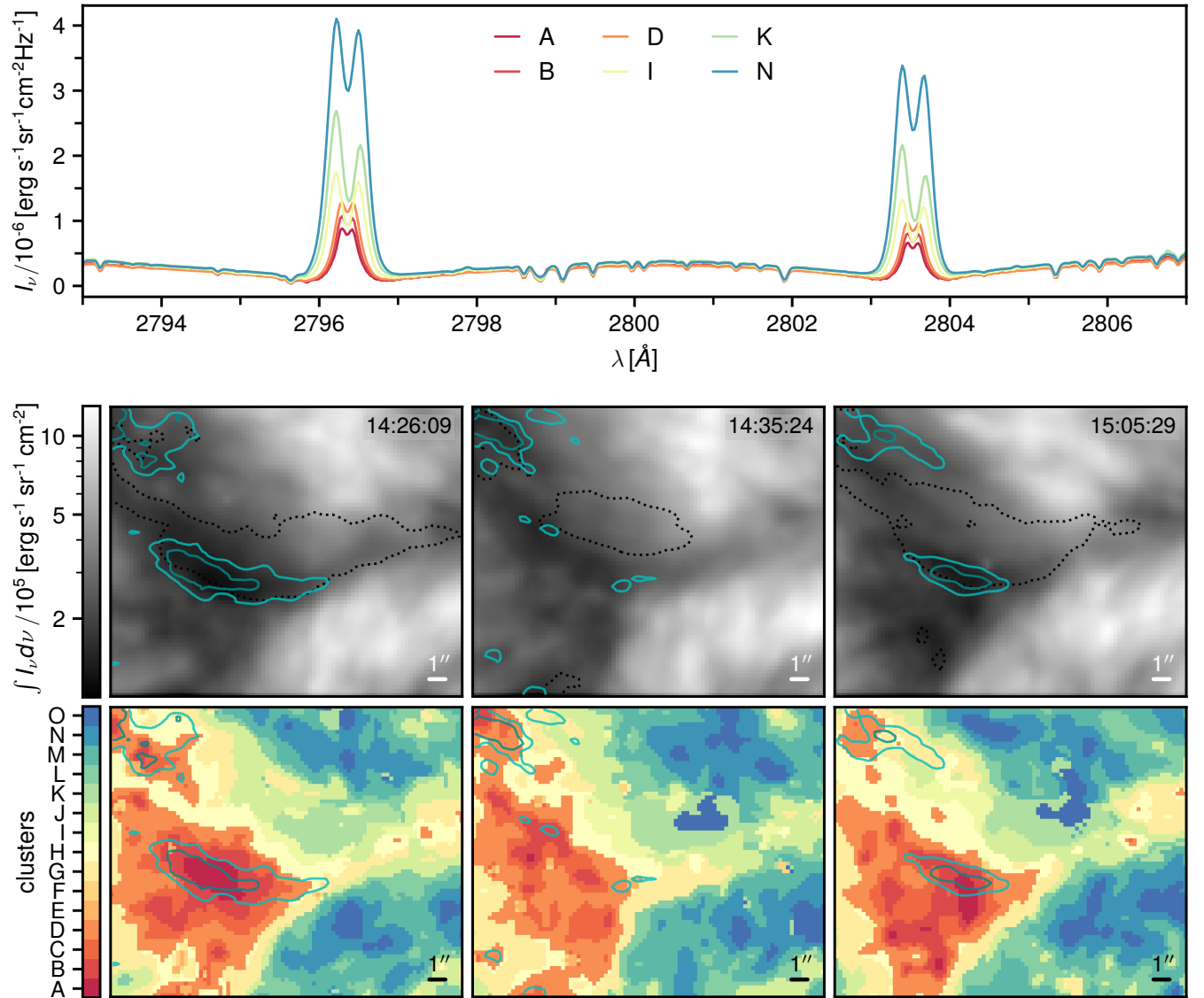


Figure 3. Clustering of Mg II h and k profiles in an AR filament. Upper panel: mean spectral profiles of selected clusters. Middle panel: integrated intensity in the k line in logarithmic scale within the region delimited by the horizontal lines in Fig. 2. Lower panel: clusters of Mg II h and k profiles. The light and dark blue contours correspond to $T_b(1.25 \text{ mm}) = 5000 \text{ K}$ and 4500 K , and the dotted black contours outline the filament boundary in the AIA 304 \AA images.

filament shows higher contrast in Band 6 than in Band 3. However, the dynamic nature of AR filaments may play a role here. The mean $T_b(3 \text{ mm})$ values within the filament identified in the 304 \AA images are around 7700 K with a few hundred-kelvin variations, which is slightly higher than the average QS level ($\sim 7500(\pm 100) \text{ K}$, White et al., 2017), but these values may be contaminated by the bright plage background because the Band 3 contours overlap with the plage as shown by the AIA 1600 \AA images. We note that the non-simultaneity of the Band 6 and Band 3 maps is relevant for interpreting relative brightness ratios.

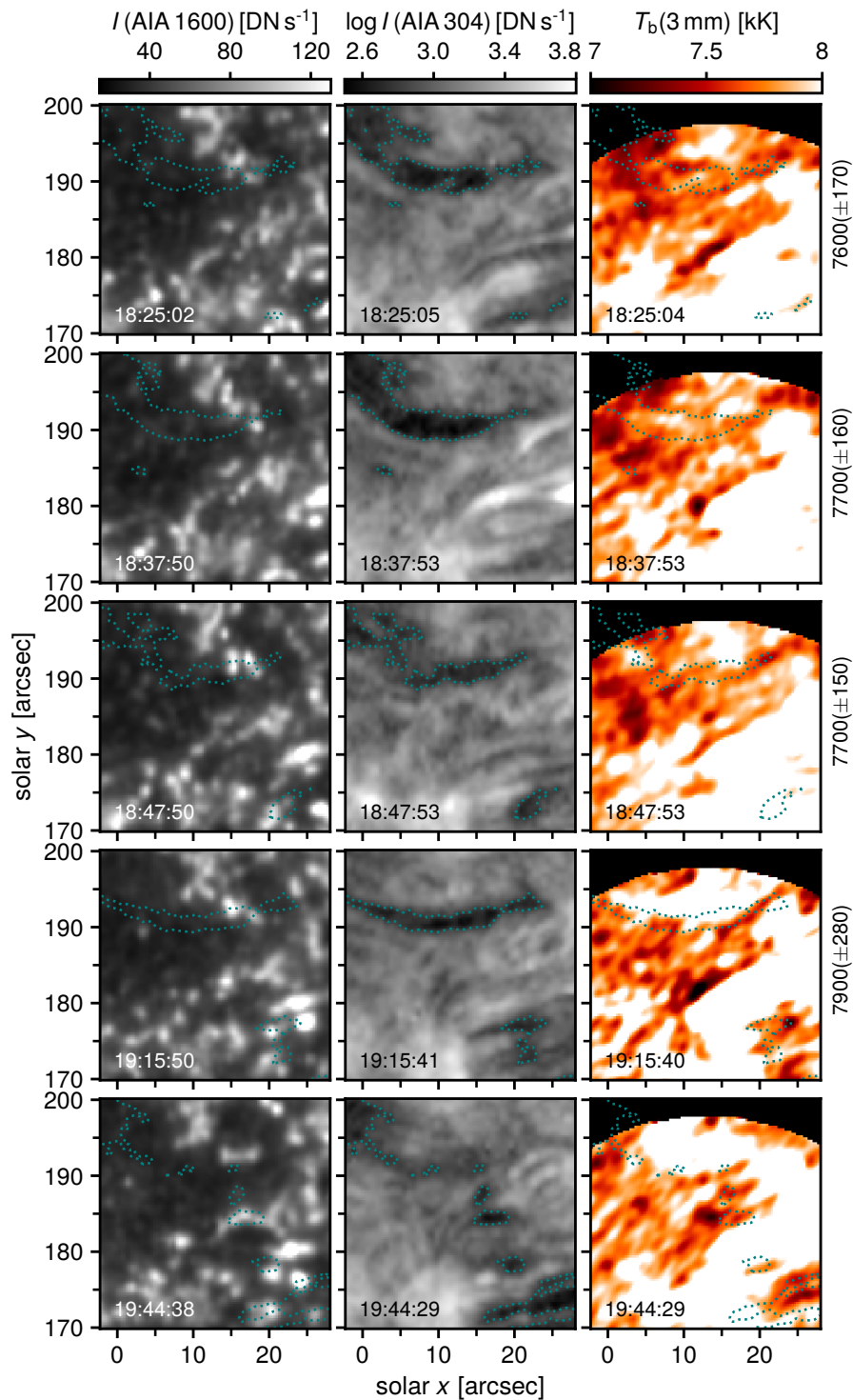


Figure 4. ALMA Band 3 observations at a later time on April 13, 2019. The ALMA colormap range is capped at 8 kK to enhance small T_b variations within the filament. Images in the AIA 1600 Å passband are displayed for context. The intensities are capped for display purposes. The cyan contours delimit the filament structure in the AIA 304 Å images. The values on the right indicate the mean(\pm standard deviation) $T_b(3\text{ mm})$ within the filament contours.

4 DISCUSSION AND CONCLUSIONS

This paper presents ALMA observations of an AR filament at two mm wavelengths supported by SDO and partly by IRIS and Hinode. The filament shows substantial temporal variability in the AIA 304 Å passband, the Mg II h and k lines, and in ALMA Band 6. Brightness variations are also detected in Band 3 but they are more difficult to discern from the background fluctuations. As anticipated, the ALMA Band 6 interferometric T_b maps show dark/cool features with much higher contrast relative to the background than the single-dish observations reported thus far (Alissandrakis et al., 2017; Brajša et al., 2018). Very fine dark threads can be seen at certain times (e.g., Fig. 2, 14:36 UT), but they do not last more than a few minutes. However, not all of the filament body (as seen by IRIS or AIA 304 Å) appears dark, but there are significant brightness variations across the filament spine. We note that the filament is also visible in the second Band 6 observing block until 17:47 UT (not displayed). We did not identify significant changes in the photospheric magnetic field that we could relate to the filament variability, but we would need field extrapolations to study the topology of the filament itself to investigate a possible correlation between "magnetic dips" and the mm continuum brightness distribution, similarly to what has been done based on $H\alpha$ observations (e.g., Aulanier et al., 1999; van Ballegoijen, 2004; Guo et al., 2010; Li et al., 2017).

We find a spatial association between the integrated k line intensity and $T_b(1.25\text{ mm})$ in the filament that is consistent in time. This suggests that both diagnostics are coupled through changes in temperature and electron density. The Mg II lines are narrower and the central reversals are shallower than the average QS profile at those locations. The coolest $T_b(1.25\text{ mm})$ values coincide with the dark structures that are visible away from the k (and h) line center and thus extend down to lower heights in the atmosphere. The lower atmosphere may be filled with low-lying dense cool threads where the absorption is high but the emissivity is low, hence the weak Mg II lines. However, interpreting the Mg II line shapes is not trivial as they depend on the interplay between the incident radiation, gas pressure, filament thickness, and the properties of the prominence-corona transition region (Heinzel et al., 2014), and thus require a follow-up investigation.

Detailed radiative transfer models of AR filaments are scarce in the literature. The spectral synthesis based on a 3D whole-prominence fine structure model presented by Gunár et al. (2016) shows filament threads in emission by a few hundred kelvins above a uniform disk background at 1.25 mm unlike what we observed; the simulated filament is optically thin ($\tau_\nu < 1$) at this wavelength. The emerging brightness temperature is the result of the absorbed background brightness temperature, T_b^{bcg} , plus the integrated emission along a geometrical path of length L :

$$T_b(\nu) = T_b^{\text{bcg}}(\nu) e^{-\tau_\nu} + \int_0^L T \kappa_\nu e^{-\int_0^l \kappa_\nu dl'} dl, \quad (1)$$

where κ_ν is the frequency-dependent absorption coefficient (e.g., Gunár et al., 2016). Brightness temperature values lower than the background level require kinetic temperatures, T , lower than background temperatures. However, the observed AR filament and background certainly have different properties than the simulated ones. Dedicated simulations with more realistic AR conditions are needed to investigate this.

Constraining both the kinetic temperature and thickness of the prominence is not possible using single-band data but it requires simultaneous observations at two wavelengths and the assumption of isothermal conditions (e.g., Heinzel et al., 2015a; Rodger and Labrosse, 2017). In that case, Eq. 1 simplifies to

$$T_b(\nu) = T_b^{\text{bcg}}(\nu) e^{-\tau_\nu} + T(1 - e^{-\tau_\nu}). \quad (2)$$

An hour after the Band 6 observations, the filament is still visible in the AIA 304 Å images, but it is indiscernible from the background in Band 3. This cannot be attributed to a difference in spatial resolution (by a factor of ~ 2) because the dark threads in the Band 6 with the typical sizes of a few arcseconds would be well resolved with Band 3. Instead, it could imply that the filament temperature is similar to the background. We note that the background is far from uniform, which makes it complicated to interpret T_b variations within the filament. Assuming that the average properties of the filament did not significantly change between the time the Band 6 and Band 3 maps were taken, which is a reasonable assumption at least for the first Band 3 observing block (Fig. 4), it is difficult to reconcile these observations with an isothermal model since we would expect even stronger absorption features at 3 mm than at 1.25 mm (see also Rodger et al., 2019). Following Dulk (1985), the opacity ratio in both bands is given by

$$\frac{\kappa_3}{\kappa_{1.25}} = \left[\frac{\nu_{1.25}}{\nu_3} \right]^2 \frac{18.2 + \ln(T^{3/2}) - \ln \nu_3}{18.2 + \ln(T^{3/2}) - \ln \nu_{1.25}}, \quad (T < 2 \times 10^5 \text{ K}). \quad (3)$$

An optically thick plasma at 3 mm with a kinetic temperature of 7500 K (equal to the mean QS background at 3 mm) would show a higher mean $T_b(1.25 \text{ mm})$ than what we have observed. For example, $\tau_{3 \text{ mm}} = 1$ implies $\tau_{1.25 \text{ mm}} = 0.15$ and $T_b(1.25 \text{ mm}) \sim 6100 \text{ K}$, which would make the filament stand out above the background. Therefore, these two wavelengths are more likely sensitive to different layers of the filament with different temperature and density conditions, or there is a temperature gradient spanning their formation heights, with Band 6 probing closer to the lowest temperatures of the filament, and Band 3 sensing warmer filament plasma or possibly the outermost shell that separates it from the corona if the optical thickness is large. Simultaneous observations of AR filaments in both ALMA bands are needed to clarify these findings.

Combined non-LTE radiative transfer modeling of the Mg II h and k lines and the radio continua will be required to diagnose the properties of the observed filament. Using such an approach, ALMA observations will allow us to constrain the plasma temperature, while the IRIS spectra can provide information about the pressure/density and the LOS velocity gradients.

REFERENCES

- Alissandrakis, C. E., Patsourakos, S., Nindos, A., and Bastian, T. S. (2017). Center-to-limb observations of the Sun with ALMA . Implications for solar atmospheric models. *A&A* 605, A78. doi:10.1051/0004-6361/201730953
- Astropy Collaboration, Price-Whelan, A. M., Sipőcz, B. M., Günther, H. M., Lim, P. L., Crawford, S. M., et al. (2018). The Astropy Project: Building an Open-science Project and Status of the v2.0 Core Package. *AJ* 156, 123. doi:10.3847/1538-3881/aabc4f
- Aulanier, G., Démoulin, P., Mein, N., van Driel-Gesztelyi, L., Mein, P., and Schmieder, B. (1999). 3-D magnetic configurations supporting prominences. III. Evolution of fine structures observed in a filament channel. *A&A* 342, 867–880
- Bastian, T. S., Ewell, J., M. W., and Zirin, H. (1993). A Study of Solar Prominences near $\lambda = 1$ Millimeter. *ApJ* 418, 510. doi:10.1086/173413
- Bražša, R., Sudar, D., Benz, A. O., Skokić, I., Bárta, M., De Pontieu, B., et al. (2018). First analysis of solar structures in 1.21 mm full-disc ALMA image of the Sun. *A&A* 613, A17. doi:10.1051/0004-6361/201730656
- Casini, R., Bevilacqua, R., and López Ariste, A. (2005). Principal Component Analysis of the He I D₃ Polarization Profiles from Solar Prominences. *ApJ* 622, 1265–1274. doi:10.1086/428283

- Chen, P.-F., Xu, A.-A., and Ding, M.-D. (2020). Some interesting topics provoked by the solar filament research in the past decade. *Research in Astronomy and Astrophysics* 20, 166. doi:10.1088/1674-4527/20/10/166
- da Silva Santos, J. M., de la Cruz Rodríguez, J., White, S. M., Leenaarts, J., Vissers, G. J. M., and Hansteen, V. H. (2020). ALMA observations of transient heating in a solar active region. *A&A* 643, A41. doi:10.1051/0004-6361/202038755
- De Pontieu, B., Title, A. M., Lemen, J. R., Kushner, G. D., Akin, D. J., Allard, B., et al. (2014). The Interface Region Imaging Spectrograph (IRIS). *Sol. Phys.* 289, 2733–2779. doi:10.1007/s11207-014-0485-y
- Díaz Baso, C. J. and Asensio Ramos, A. (2018). Enhancing SDO/HMI images using deep learning. *A&A* 614, A5. doi:10.1051/0004-6361/201731344
- Díaz Baso, C. J., Martínez González, M. J., Asensio Ramos, A., and de la Cruz Rodríguez, J. (2019). Diagnostic potential of the Ca II 8542 Å line for solar filaments. *A&A* 623, A178. doi:10.1051/0004-6361/201834793
- Dulk, G. A. (1985). Radio emission from the sun and stars. *ARA&A* 23, 169–224. doi:10.1146/annurev.aa.23.090185.001125
- Freeland, S. L. and Handy, B. N. (1998). Data Analysis with the SolarSoft System. *Sol. Phys.* 182, 497–500. doi:10.1023/A:1005038224881
- Gibson, S. E. (2018). Solar prominences: theory and models. Fleshing out the magnetic skeleton. *Living Reviews in Solar Physics* 15, 7. doi:10.1007/s41116-018-0016-2
- Gunár, S., Heinzel, P., Anzer, U., and Mackay, D. H. (2018). Quiescent Prominences in the Era of ALMA. II. Kinetic Temperature Diagnostics. *ApJ* 853, 21. doi:10.3847/1538-4357/aaa001
- Gunár, S., Heinzel, P., Mackay, D. H., and Anzer, U. (2016). Quiescent Prominences in the Era of ALMA: Simulated Observations Using the 3D Whole-prominence Fine Structure Model. *ApJ* 833, 141. doi:10.3847/1538-4357/833/2/141
- Guo, Y., Schmieder, B., Démoulin, P., Wiegmann, T., Aulanier, G., Török, T., et al. (2010). Coexisting Flux Rope and Dipped Arcade Sections Along One Solar Filament. *ApJ* 714, 343–354. doi:10.1088/0004-637X/714/1/343
- Harrison, R. A., Carter, M. K., Clark, T. A., Lindsey, C., Jefferies, J. T., Sime, D. G., et al. (1993). An active solar prominence in 1.3 MM radiation. *A&A* 274, L9
- Harvey, J. W., Bolding, J., Clark, R., Hauth, D., Hill, F., Kroll, R., et al. (2011). Full-disk Solar H-alpha Images From GONG. In *AAS/Solar Physics Division Abstracts #42*. vol. 42 of *AAS/Solar Physics Division Meeting*, 17.45
- Heinzel, P., Berlicki, A., Bárta, M., Karlický, M., and Rudawy, P. (2015a). On the Visibility of Prominence Fine Structures at Radio Millimeter Wavelengths. *Sol. Phys.* 290, 1981–2000. doi:10.1007/s11207-015-0719-7
- Heinzel, P., Berlicki, A., Bárta, M., Rudawy, P., Gunár, S., Labrosse, N., et al. (2022). ALMA as a prominence thermometer: First observations. *arXiv e-prints*, arXiv:2202.12761
- Heinzel, P., Schmieder, B., Mein, N., and Gunár, S. (2015b). Understanding the Mg II and H α Spectra in a Highly Dynamical Solar Prominence. *ApJ* 800, L13. doi:10.1088/2041-8205/800/1/L13
- Heinzel, P., Vial, J. C., and Anzer, U. (2014). On the formation of Mg ii h and k lines in solar prominences. *A&A* 564, A132. doi:10.1051/0004-6361/201322886
- Jejčič, S., Schwartz, P., Heinzel, P., Zapiór, M., and Gunár, S. (2018). Statistical analysis of UV spectra of a quiescent prominence observed by IRIS. *A&A* 618, A88. doi:10.1051/0004-6361/201833466

- Kuckein, C., Centeno, R., Martínez Pillet, V., Casini, R., Manso Sainz, R., and Shimizu, T. (2009). Magnetic field strength of active region filaments. *A&A* 501, 1113–1121. doi:10.1051/0004-6361/200911800
- Kuckein, C., Martínez Pillet, V., and Centeno, R. (2012). An active region filament studied simultaneously in the chromosphere and photosphere. I. Magnetic structure. *A&A* 539, A131. doi:10.1051/0004-6361/201117675
- Kundu, M. R. (1972). Observations of Prominences at 3.5 Millimeter Wavelength. *Sol. Phys.* 25, 108–115. doi:10.1007/BF00155749
- Labrosse, N., Heinzl, P., Vial, J. C., Kucera, T., Parenti, S., Gunár, S., et al. (2010). Physics of Solar Prominences: I—Spectral Diagnostics and Non-LTE Modelling. *Space Sci. Rev.* 151, 243–332. doi:10.1007/s11214-010-9630-6
- Labrosse, N., Rodger, A. S., Radziszewski, K., Rudawy, P., Antolin, P., Fletcher, L., et al. (2022). First High Resolution Interferometric Observation of a Solar Prominence With ALMA. *arXiv e-prints*, arXiv:2202.12434
- Lemen, J. R., Title, A. M., Akin, D. J., Boerner, P. F., Chou, C., Drake, J. F., et al. (2012). The Atmospheric Imaging Assembly (AIA) on the Solar Dynamics Observatory (SDO). *Sol. Phys.* 275, 17–40
- Leroy, J. L. (1989). Observation of prominence magnetic fields. In *Dynamics and Structure of Quiescent Solar Prominences*, ed. E. R. Priest. vol. 150 of *Astrophysics and Space Science Library*, 77–113. doi:10.1007/978-94-009-3077-3_13
- Levens, P. J. and Labrosse, N. (2019). Modelling of Mg II lines in solar prominences. *A&A* 625, A30. doi:10.1051/0004-6361/201833132
- Li, S., Su, Y., Zhou, T., van Ballegoijen, A., Sun, X., and Ji, H. (2017). High-resolution Observations of Sympathetic Filament Eruptions by NVST. *ApJ* 844, 70. doi:10.3847/1538-4357/aa78f5
- Lindsey, C. (1994). The Sun in Submillimeter Radiation. In *Infrared Solar Physics*, eds. D. M. Rabin, J. T. Jefferies, and C. Lindsey. vol. 154, 85
- Lites, B. W. and Ichimoto, K. (2013). The SP_PREP Data Preparation Package for the Hinode Spectro-Polarimeter. *Sol. Phys.* 283, 601–629. doi:10.1007/s11207-012-0205-4
- McMullin, J. P., Waters, B., Schiebel, D., Young, W., and Golap, K. (2007). CASA Architecture and Applications. In *Astronomical Data Analysis Software and Systems XVI*, eds. R. A. Shaw, F. Hill, and D. J. Bell. vol. 376 of *Astronomical Society of the Pacific Conference Series*, 127
- Orozco Suárez, D., Asensio Ramos, A., and Trujillo Bueno, J. (2014). The magnetic field configuration of a solar prominence inferred from spectropolarimetric observations in the He I 10 830 Å triplet. *A&A* 566, A46. doi:10.1051/0004-6361/201322903
- Parenti, S. (2014). Solar Prominences: Observations. *Living Reviews in Solar Physics* 11, 1. doi:10.12942/lrsp-2014-1
- Peat, A. W., Labrosse, N., Schmieder, B., and Barczynski, K. (2021). Solar prominence diagnostics from non-LTE modelling of Mg II h&k line profiles. *A&A* 653, A5. doi:10.1051/0004-6361/202140907
- Pesnell, W. D., Thompson, B. J., and Chamberlin, P. C. (2012). The Solar Dynamics Observatory (SDO). *Sol. Phys.* 275, 3–15
- Poduval, B., DeForest, C. E., Schmelz, J. T., and Pathak, S. (2013). Point-spread Functions for the Extreme-ultraviolet Channels of SDO/AIA Telescopes. *ApJ* 765, 144. doi:10.1088/0004-637X/765/2/144
- Raoult, A., Lantos, P., and Fuerst, E. (1979). Prominences at centrimetric and millimetric wavelengths. I. Size and spectrum of the radio filaments. *Sol. Phys.* 61, 335–343. doi:10.1007/BF00150418
- Rodger, A. and Labrosse, N. (2017). Solar Prominence Modelling and Plasma Diagnostics at ALMA Wavelengths. *Sol. Phys.* 292, 130. doi:10.1007/s11207-017-1161-9

- Rodger, A. S., Labrosse, N., Wedemeyer, S., Szydlarski, M., Simões, P. J. A., and Fletcher, L. (2019). First Spectral Analysis of a Solar Plasma Eruption Using ALMA. *ApJ* 875, 163. doi:10.3847/1538-4357/aafdfb
- Ruan, G., Ježič, S., Schmieder, B., Mein, P., Mein, N., Heinzl, P., et al. (2019). Diagnostics of the Prominence Plasma from H α and Mg II Spectral Observations. *ApJ* 886, 134. doi:10.3847/1538-4357/ab4b50
- Scherrer, P. H., Schou, J., Bush, R. I., Kosovichev, A. G., Bogart, R. S., Hoeksema, J. T., et al. (2012). The Helioseismic and Magnetic Imager (HMI) Investigation for the Solar Dynamics Observatory (SDO). *Sol. Phys.* 275, 207–227
- Schmahl, E. J., Bobrowsky, M., and Kundu, M. R. (1981). Observations of Solar Filaments at 8-GHZ 15-GHZ 22-GHZ and 43-GHZ. *Sol. Phys.* 71, 311–328. doi:10.1007/BF00167554
- Schmieder, B., Tian, H., Kucera, T., López Ariste, A., Mein, N., Mein, P., et al. (2014). Open questions on prominences from coordinated observations by IRIS, Hinode, SDO/AIA, THEMIS, and the Meudon/MSDP. *A&A* 569, A85. doi:10.1051/0004-6361/201423922
- Stellmacher, G., Wiehr, E., and Dammasch, I. E. (2003). Spectroscopy of Solar Prominences Simultaneously From Space and Ground. *Sol. Phys.* 217, 133–155. doi:10.1023/A:1027310303994
- The SunPy Community, Barnes, W. T., Bobra, M. G., Christe, S. D., Freij, N., Hayes, L. A., et al. (2020). The sunpy project: Open source development and status of the version 1.0 core package. *The Astrophysical Journal* 890, 68–. doi:10.3847/1538-4357/ab4f7a
- Tsuneta, S., Ichimoto, K., Katsukawa, Y., Nagata, S., Otsubo, M., Shimizu, T., et al. (2008). The Solar Optical Telescope for the Hinode Mission: An Overview. *Sol. Phys.* 249, 167–196. doi:10.1007/s11207-008-9174-z
- van Ballegoijen, A. A. (2004). Observations and Modeling of a Filament on the Sun. *ApJ* 612, 519–529. doi:10.1086/422512
- Vial, J. C., Zhang, P., and Buchlin, É. (2019). Some relationships between radiative and atmospheric quantities through 1D NLTE modeling of prominences in the Mg II lines. *A&A* 624, A56. doi:10.1051/0004-6361/201834249
- Virtanen, P., Gommers, R., Oliphant, T. E., Haberland, M., Reddy, T., Cournapeau, D., et al. (2020). SciPy 1.0: Fundamental Algorithms for Scientific Computing in Python. *Nature Methods* 17, 261–272. doi:10.1038/s41592-019-0686-2
- Vrsnak, B., Pohjolainen, S., Urpo, S., Terasranta, H., Brajsa, R., Ruzdjak, V., et al. (1992). Large-scale patterns on the Sun observed in the millimetric wavelength range. *Sol. Phys.* 137, 67–86. doi:10.1007/BF00146576
- Ward, J. H. (1963). Hierarchical grouping to optimize an objective function. *Journal of the American Statistical Association* 58, 236–244. doi:10.1080/01621459.1963.10500845
- Wedemeyer, S., Bastian, T., Brajša, R., Hudson, H., Fleishman, G., Loukitcheva, M., et al. (2016). Solar Science with the Atacama Large Millimeter/Submillimeter Array—A New View of Our Sun. *Space Sci. Rev.* 200, 1–73. doi:10.1007/s11214-015-0229-9
- White, S. M., Iwai, K., Phillips, N. M., Hills, R. E., Hirota, A., Yagoubov, P., et al. (2017). Observing the Sun with the Atacama Large Millimeter/submillimeter Array (ALMA): Fast-Scan Single-Dish Mapping. *Sol. Phys.* 292, 88. doi:10.1007/s11207-017-1123-2
- Wooten, A. and Thompson, A. R. (2009). The Atacama Large Millimeter/Submillimeter Array. *IEEE Proceedings* 97, 1463–1471. doi:10.1109/JPROC.2009.2020572
- Xu, Z., Lagg, A., Solanki, S., and Liu, Y. (2012). Magnetic Fields of an Active Region Filament from Full Stokes Analysis of Si I 1082.7 nm and He I 1083.0 nm. *ApJ* 749, 138. doi:10.1088/0004-637X/749/2/138

CONFLICT OF INTEREST STATEMENT

The authors declare that the research was conducted in the absence of any commercial or financial relationships that could be construed as a potential conflict of interest.

AUTHOR CONTRIBUTIONS

JS, SW, and JL contributed to the ALMA research proposal and data acquisition. SW performed the ALMA data reduction. JS conducted the analysis. JS, SW, KR, GC, SG, PH, and JL contributed to the discussion and writing.

FUNDING

SG and PH acknowledge support from the grants 19-16890S and 19-17102S of the Czech Science Foundation (GAČR). SG and PH thank for the support from project RVO:67985815 of the Astronomical Institute of the Czech Academy of Sciences.

ACKNOWLEDGMENTS

This paper makes use of the following ALMA data: ADS/JAO.ALMA#2018.1.01518.S. ALMA is a partnership of ESO (representing its member states), NSF (USA) and NINS (Japan), together with NRC (Canada), MOST and ASIAA (Taiwan), and KASI (Republic of Korea), in cooperation with the Republic of Chile. The Joint ALMA Observatory is operated by ESO, AUI/NRAO and NAOJ. IRIS is a NASA small explorer mission developed and operated by LMSAL with mission operations executed at NASA Ames Research center and major contributions to downlink communications funded by ESA and the Norwegian Space Centre. Hinode is a Japanese mission developed and launched by ISAS/JAXA, with NAOJ as domestic partner and NASA and STFC (UK) as international partners. It is operated by these agencies in co-operation with ESA and NSC (Norway). Data were acquired by GONG instruments operated by NISP/NSO/AURA/NSF with contribution from NOAA. The NSO is operated by the Association of Universities for Research in Astronomy, Inc., under cooperative agreement with the National Science Foundation. This research has made use of *Astropy* (<https://astropy.org>) – a community-developed core Python package for Astronomy (Astropy Collaboration et al., 2018), *SunPy* (<https://sunpy.org>) – an open-source and free community-developed solar data analysis Python package (The SunPy Community et al., 2020), and MATLAB and the Image Processing Toolbox release 2021b (The Mathworks, Inc., Natick, MA, USA).

DATA AVAILABILITY STATEMENT

The SDO data can be obtained from the Joint Science Operations Center (<http://jsoc.stanford.edu>). The IRIS data can be downloaded from the Heliophysics Events Knowledgebase Coverage Registry (<https://www.lmsal.com/hek/hcr>). The Hinode data can be obtained from the Community Spectro-polarimetric Analysis Center (<http://www2.hao.ucar.edu/csac>). The GONG data can be fetched from Data Archive (<https://gong2.nso.edu/archive>). The raw ALMA data can be found at the ALMA Science Archive (<https://almascience.nrao.edu/aq>).